Materials Advances

COMMUNICATION

View Article Online
View Journal | View Issue

Cite this: *Mater. Adv.*, 2025, 6, 954

Received 21st July 2024,
Accepted 27th December 2024

DOI: 10.1039/d4ma00735b

rsc.li/materials-advances

Layered $NbOCl_2$ kinetic degradation mechanism and improved second-order nonlinear optical responses†

Jianlong Kang,[ab] Yiduo Wang,[ab] Li Zhou,[ab] Ahmed Asad,[ab] Defeng Xu,[ab] Zhihui Chen,[ab] Yingwei Wang, *[ab] Jun He[ab] and Si Xiao *[ab]

$NbOCl_2$ exhibits exceptional nonlinear optical response, particularly for second harmonic generation (SHG). However, the environmental degradation mechanism of $NbOCl_2$ remains incompletely understood, posing challenges to device stability and optimization. This work demonstrates the kinetic degradation mechanism of 2D layered $NbOCl_2$ and proposes a strategy to improve the stability of nano-sized materials. It is primarily driven by the preferential replacement of Cl^- ions in $NbOCl_2$ with OH^- ions, which is regulated by storage temperature and H^+ ions in the solution. Notably, the SHG response can be tuned effectively by altering the excitation power, degradation time, and irradiation wavelength. Additionally, the significant SHG of the $NbOCl_2$ nanosheets is remarkably stable when protected by poly methyl methacrylate. These findings offer novel insights into kinetic degradation mechanisms and strategies to improve the stability of $NbOCl_2$.

1. Introduction

Material stability is a key property of wavelength conversion in nonlinear optical devices with applications in areas, such as laser devices,[1] microwave sensors,[2] and quantum light.[3] With the current trends of on-chip integration of functional devices, there is an increasing demand for high conversion efficiency, stability, and reduced dimensions.[4] Due to its unique twisted structure, $NbOCl_2$ has excellent SHG properties, and thus, it has attracted considerable research interest.[5] $NbOCl_2$ nanosheets have high up-conversion efficiency (0.004%),[6] with the strongest anisotropic SHG emission intensity along the polar axis.[7] Further efficiency and enhancement of emission intensity can be achieved through tensile strain and anion alloying techniques.[5,8] The non-zero acentric displacement of Nb atoms forms two short and two long Nb–X bonds.[9,10] The Nb–Nb pairs form a first-order Peierls distortion that can withstand high-temperature thermal fluctuations.[6,11] This unique structure enables $NbOCl_2$ to exhibit excellent anisotropic properties,[12] such as the carrier mobilities of electrons and holes,[13–16] strong size-related light absorption,[17] and mechanical response.[6] However, its chemical stability poses a significant challenge in the construction of micro- and nano-devices and integration process.[3]

Currently, the degradation mechanism of $NbOCl_2$ remains unclear, making it more difficult to proactively formulate strategies for the design, manufacture, and long-term industrial applications of devices. Typically, water or oxygen are considered to be key factors influencing material stability, as observed in other materials, such as BP,[18] graphene,[19] and TiS_2.[20] Unfortunately, the long-term working environments of nonlinear crystals often cannot completely isolate these factors, and the degradation mechanisms are scarcely investigated. Furthermore, $NbOCl_2$ possesses unique electronic properties and strong ionic Cl–Nb bonds,[3] rendering the comprehensive analysis of its degradation mechanism exceedingly difficult. In comparison to methods, such as mechanical exfoliation[6] and chemical vapor transport,[10] liquid-phase exfoliation (LPE)[21] methods are reported less for controlling the downsizing of $NbOCl_2$, yet they offer numerous operational advantages.[22]

This work reports excellent SHG response from few-layer $NbOCl_2$ nanosheets prepared *via* LPE, with *N*-methyl-2-pyrrolidone (NMP) environment being the most recommended for use around it. Experimentally, a deeper level of degradation mechanism is proposed and verified, which indicates OH^- ions generated from water ionization to be the primary driving force, surpassing the influence of water or oxygen. The degradation process is temperature-controlled, which is slowed down by H^+ ions. Degradation of $NbOCl_2$ gradually weakens the strong SHG response until it becomes negligible, whereas $NbOCl_2$ that is protected by poly methyl methacrylate (PMMA) exhibits outstanding SHG stability. This difference presents an effective improvement strategy for the

[a] *Hunan Key Laboratory of Nanophotonics and Devices, School of Physics, Central South University, Changsha 410083, People's Republic of China. E-mail: wyw1988@csu.edu.cn, sixiao@csu.edu.cn*

[b] *Hunan Key Laboratory for Super-microstructure and Ultrafast Process, School of Physics, Central South University, 932 South Lushan Road, Changsha, Hunan 410083, People's Republic of China*

† Electronic supplementary information (ESI) available. See DOI: https://doi.org/10.1039/d4ma00735b

on-chip integration of $NbOCl_2$ nanosheets into nonlinear optical devices and liquid-phase environments.

2. Experimental

2.1. Materials

Bulk $NbOCl_2$ was procured from Nanjing MKNANO Tech. Co., Ltd. Solvents, including NMP, isopropanol (IPA), dimethylformamide (DMF), and ethanol (EtOH), along with HCl and KOH solids, were obtained from MACKLIN. Poly methyl methacrylate (PMMA, $M_w \sim 350\,000$) and methacide ($C_6H_5CH_3$, 99.8%) were bought from Sigma-Aldrich.

2.2. Sample preparation

The yield of $NbOCl_2$ prepared by LPE in different dispersants, such as IPA, NMP, DMF, EtOH, and water, was determined by the relationship between concentration and extinction spectral intensity. In a 60-ml sample vial, 50 mg of bulk $NbOCl_2$ was gently introduced with 50 ml of dispersing agent. A dispersion of nanosheets/bulks was obtained after 40 hours of ultrasound treatment (with proper sealing) at 80% power in a 1400 W ultrasonic bath and a low temperature (10 °C) (Fig. 1a). The mixed dispersion was centrifuged at 3000 rpm for 5 minutes. Moreover, the supernatant was centrifugated at 12 000 rpm for 20 minutes to obtain the sediment of nanosheets.[21] The sediment was resuspended to obtain the sample shown in Fig. 2. The degradation mechanism samples were obtained by centrifugation at varying parameters, ranging from 3000 rpm for 5 minutes to 6000 rpm for 20 minutes. For the organic elemental analysis, a relatively large amount of material was required to characterize hydrogen. Thus, we fully hydrolyzed 200 mg of $NbOCl_2$ bulk material and obtained the powder by freeze-drying. The SHG samples were obtained using

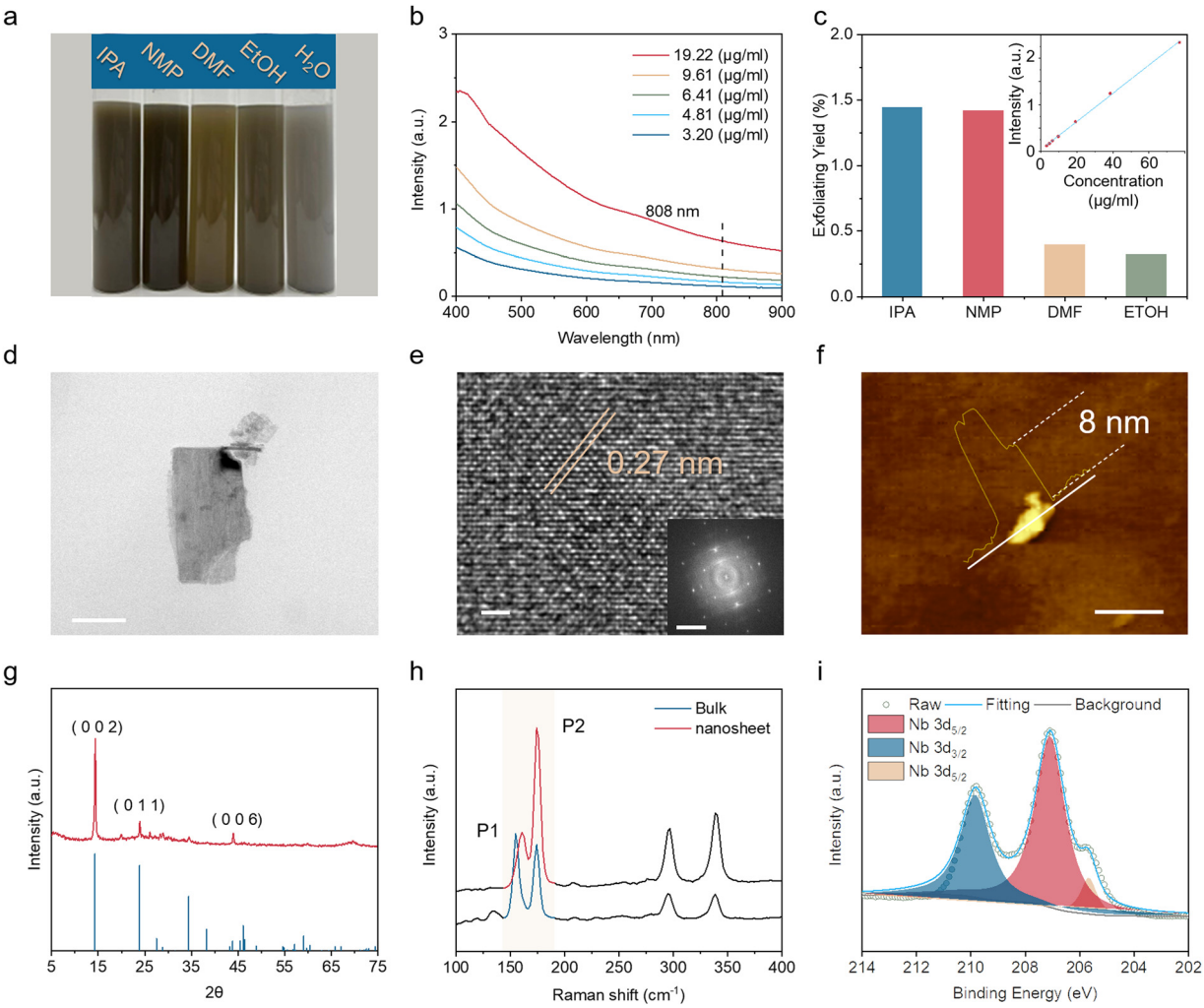

Fig. 1 (a) Optical photographs of bulk $NbOCl_2$ dispersed in different solvents after 40 hours of sonication in a water bath. (b) Extinction spectra of $NbOCl_2$ nanosheets with different concentrations. (c) Exfoliation yield of $NbOCl_2$ nanosheets in various solvents. The inset shows the extinction coefficient as a function of $NbOCl_2$ nanosheet concentration at 808 nm. (d) The TEM image of $NbOCl_2$ nanosheets (scale bar: 200 nm). (e) A high-resolution TEM image (scale bar: 1 nm) of $NbOCl_2$ nanosheets with selected area electron diffraction (scale bar: 5 nm) as an inset. (f) AFM images of multiple $NbOCl_2$ nanosheets with height information (scale bar: 250 nm). (g) An XRD spectrum of $NbOCl_2$ nanosheets. (h) Raman spectra of $NbOCl_2$ with bulk morphology and nanosheet structure (laser wavelength: 532 nm). (i) Shows the XPS spectra of Nb 3d.

centrifugation parameters ranging from 6000 rpm to 9000 rpm for 20 minutes.

PMMA encapsulation: 500 mg of PMMA were mixed with 10 ml of toluene. The mixture was then stirred with a magnetic stirrer at a low temperature until the PMMA was completely dissolved. The high-concentration solution of $NbOCl_2$ nanosheet/IPA was thoroughly mixed with the PMMA solution. The resulting mixture was then applied onto glass substrates using a spin-coater (model KW-4A) at a speed of 300 rpm for 10 s. After coating, the samples were subjected to an annealing process at a temperature of 90 °C for 5 minutes to ensure proper curing and film formation.

2.3. Configuration of the pH

For a robust acidic environment, 2 ml of concentrated hydrochloric acid was added to 50 ml of pure water to achieve a pH value lower than 1. For a strong alkali environment, 200 mg of KOH was added to 50 ml of pure water to attain a pH value higher than 14. Significant precipitation was observed in acidic environments, while no significant precipitation occurred in alkaline environments.

2.4. System for SHG characterization

The Yb-based femtosecond laser system (Pharos PH2-20W) generated a laser beam with a duration of 200 fs and a repetition rate of 0.1 MHz. The laser beam underwent initial filtration through a long-pass filter before being focused on the sample stage. The data were acquired using a monochromator (Princeton Instruments, Spectra Pro HRS500) connected to a CCD (Princeton Instruments, Pixis 400B). Measurements were acquired with no optical damage to the sample (SHG signal intensity does not decrease significantly with continuous excitation).

3. Results and discussion

3.1. Characterization

$NbOCl_2$ belongs to the $NbOX_2$ family (X = Cl, Br, or I),[9,23] which in turn belongs to the larger MOX_2 family (M = V, Nb, Mo, and Ta, X = Cl, Br, and I).[24,25] The enthalpy of formation for $NbOCl_2$ is -185 ± 1 kcal.[26] This study presents a universal LPE method for producing high-quality, few-layer, or even monolayer $NbOCl_2$ nanosheets. This method is compared with traditional bulk exfoliation using various dispersants, including NMP, IPA, DMF, EtOH, and water. Interestingly, $NbOCl_2$ dispersion in water was the only one to exhibit a white-gray colour after sonication in optical imaging (Fig. 1a), suggesting potential degradation during exfoliation in this medium. Thus, by examining the color of the sample in optical photographs, we can preliminarily determine whether there is a significant amount of impurities, such as degraded $NbOCl_2$. Inductively coupled plasma optical emission spectrometry was then used to determine the concentration of $NbOCl_2$ nanosheets in each dispersion. The extinction coefficient of $NbOCl_2$ was determined to be 30.26 L cm^{-1} g^{-1} as derived from the extinction spectra at 808 nm using Lambert–Beer's law (Fig. 1b, inset in Fig. 1c).[27] As illustrated in Fig. 1c, it is evident that both the NMP (1.42%) and IPA (1.44%) dispersants exhibit higher exfoliation efficiency, compared to the DMF (0.4%) and EtOH (0.32%) dispersants. It should be noted that strict sealing conditions are crucial during ultrasonic exfoliation and water bath sonication. Otherwise, exposure to moisture in the air could result in material degradation (especially in ETOH).

The transmission electron microscope (TEM) imaging reveals rectangular thin sheets with sharp edges, as shown in Fig. 1d. This observation may be because $NbOCl_2$ has different Young's moduli along its polar and nonpolar axes.[6,28] The crystalline properties of the nanosheets were further validated *via* a high-resolution transmission electron microscope (HRTEM) and selected area electron diffraction (SAED) spectroscopy. In the HRTEM image (Fig. 1e), a lattice spacing of 0.27 nm is observable in the marked area, which is consistent with that of the $NbOCl_2$ (103) plane (Fig. S1, ESI†). Atomic force microscopy (AFM) was used to characterize the thickness of the nanosheets (Fig. 1f). The thickness distribution exhibits a stair-step pattern, with an initial platform that is $\sim$8 nm thick. It corresponds to $\sim$12 layers of $NbOCl_2$, considering an interlayer spacing of 0.65 nm.[3] The X-ray diffraction (XRD) spectrum of $NbOCl_2$ nanosheets in Fig. 1g was obtained *via* LPE, and it closely matches the standard PDF card #87-2124. The few-layer $NbOCl_2$ nanosheets display the space groups of lmmm (71), which is consistent with previous research findings.[3] Raman spectroscopy identified prominent peaks in the bulk $NbOCl_2$ and its nanosheets (Fig. 1h). The bulk material exhibits peaks at 154.8 cm^{-1} and 174.2 cm^{-1}, while the nanosheets show one peak at a slightly shifted position, 160.6 cm^{-1}, but the second peak is the same, 174.2 cm^{-1}. The ratio of the intensity of P1 and P2 peaks in the marked region of the Raman spectrum can be used to calibrate the in-plane anisotropy exhibited by the lattice vibrations (Fig. 1h and Fig. S2, ESI†).[15] It is noteworthy that the P1 peak, attributed to the A-symmetry mode, exhibits a blue shift in the multi-layer nanosheets as compared to the bulk material. The P2 peak that corresponds to out-of-plane vibrations shows no notable change.[3] The component and chemical state were delineated by the X-ray photoelectron spectroscopy (XPS) of $NbOCl_2$ nanosheets (Fig. 1i and Fig. S3, ESI†). The binding energy spectra of Cl 2p clearly show major peaks at 200.3 and 198.7 eV, corresponding to Cl $2p_{1/2}$ and Cl $2p_{3/2}$, respectively (Fig. S3a, ESI†).[29] The binding energy spectrum of O 1s has distinct main peaks at 530.24 and 531.93 eV, which were reported in the literature to be closely related to lattice and surface hydroxyl oxygen atoms (Fig. S3b, ESI†).[30–32] The high-resolution Nb 3d XPS core spectra revealed three distinct chemical compositions. The 209.8 and 207.1 eV peaks correspond to Nb $3d_{5/2}$ and Nb $3d_{3/2}$ (5+ or Nb in the V oxidation state),[33–35] respectively. Moreover, the peak at 205.66 eV was associated with Nb +4 (Fig. 1i).[36–38]

3.2. Environmental stability

To evaluate the stability of $NbOCl_2$ nanosheets obtained through LPE (agent: NMP), the extinction spectra were monitored over time in various dispersants (Fig. S4, ESI†).[39,40]

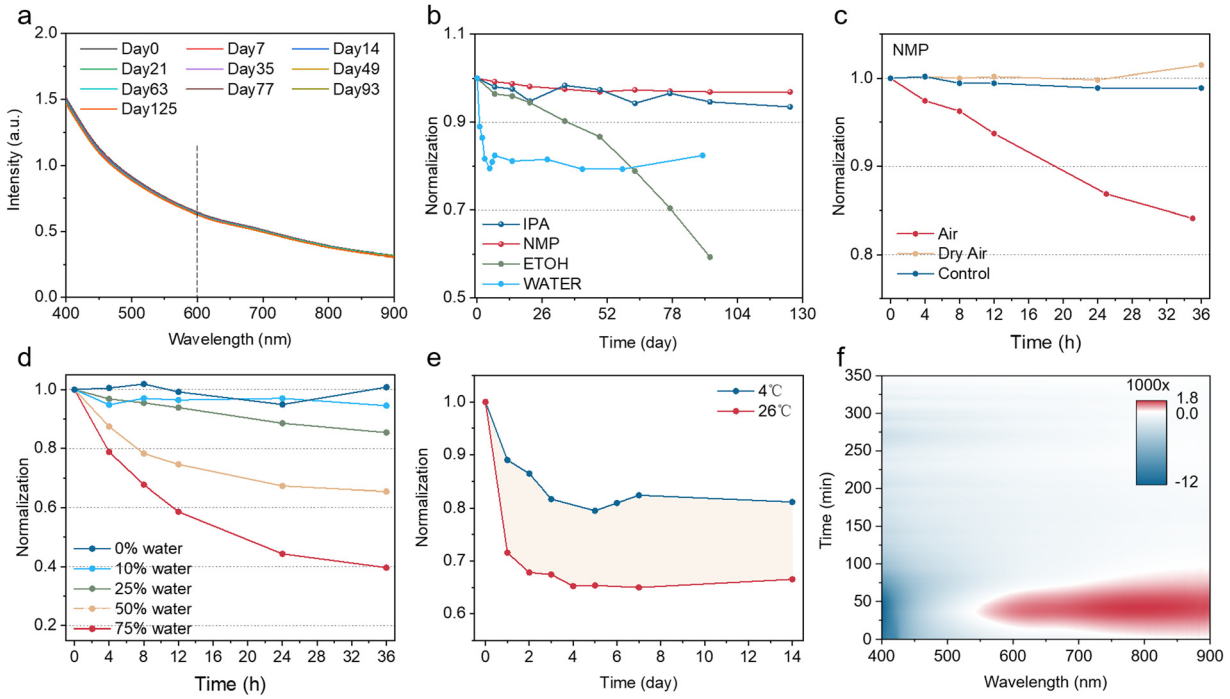

Fig. 2 (a) The extinction spectra of $NbOCl_2$ nanosheets dispersed in NMP solvent after storage at 4 °C for different durations. (b) The percentage of intensity at 600 nm (A/A_0) for different solvents varies with storage durations at 4 °C. A is the intensity at various times, and A_0 is the original value. (c) Intensity normalization at 600 nm of spectra for groups with different air content as a function of time. (d) Plot of the time-dependent intensity normalization at 600 nm across spectra of groups with distinct water content. (e) The variation in the intensity percentage at 600 nm with respect to different storage times observed under controlled temperature. (f) 2D colour mapping of the extinction spectra of $NbOCl_2$ nanosheet degradation.

Fig. 2a shows the UV/vis spectra of $NbOCl_2$ nanosheets in NMP dispersant stored at 4 °C, which was recorded at various time points. Additionally, Fig. 2b depicts the intensity of the extinction spectra at 600 nm tracked for $NbOCl_2$ nanosheet suspensions in various solvents, including IPA, NMP, DMF, EtOH, and water. For comparison, the absorbance values were normalized to the initial measurement obtained during the first UV/vis measurement. These measurements revealed excellent stability in NMP and IPA, while noticeable changes were observed in the extinction spectra obtained in water (Fig. S4d, ESI†) and EtOH (Fig. S4b, ESI†) suspensions. Particularly, when the nanosheets were stored in water, the degradation of $NbOCl_2$ nanosheets occurred rapidly, resulting in a drastic change in the extinction spectra over a short time. Optical images of samples stored with sealed organic dispersants at different time points showed no noticeable colour change, but samples stored in water showed obvious colour changes (Fig. S4e, ESI†). Similar oxygen or water-induced degradation phenomena have also been previously reported in other 2D material systems (BP,[18] MXenes,[41] VSe,[42] Nb[43]).

The influence of water or oxygen on $NbOCl_2$ degradation was investigated by monitoring the extinction spectra of three sample groups at various time points: samples exposed to humid air, samples exposed to dry air, and an untreated control group (Fig. 2c and Fig. S5, ESI†).[18,20] The results strongly suggest that water is the primary factor triggering the degradation reaction of $NbOCl_2$, rather than oxygen. To further substantiate the role of water in the degradation of the $NbOCl_2$ nanosheet, extinction spectra were monitored for $NbOCl_2$ dispersed in NMP solutions with varying water contents (Fig. 2d and Fig. S6, ESI†). The results showed a significant acceleration in the degradation rate of $NbOCl_2$ nanosheets with increasing water content. The results can be fitted by an exponential decay function:

$$y = A_1 * \exp(-t/\tau) + y_0 \quad (1)$$

where τ is the time constant. For samples with 25%, 50%, and 75% water content, τ can be reasonably fitted to 41.0 h, 14.7 h, and 10.8 h, respectively. Additionally, the influence of storage temperature on the degradation of $NbOCl_2$ nanosheets was examined under consistent conditions with respect to other experimental parameters (Fig. 2e and Fig. S7, ESI†). The results suggest that the degradation rate of $NbOCl_2$ nanosheets decreases at lower temperatures, promoting long-term storage stability ($\tau_{4\,°C}$: 1.53 day; $\tau_{26\,°C}$: 0.58 day). Time-resolved extinction spectra were measured to further investigate the degradation reaction of $NbOCl_2$ nanosheets at a concentration of 24.7 ppm, allowing for the creation of a 2D colour map (Fig. S8a, ESI†). Upon conducting first-order derivative processing on the images, it was observed that $NbOCl_2$ exhibited a sharp positive derivative region across the wavelength range between 550 nm and 900 nm (Fig. 2f and Fig. S8b, ESI†). This positive signal may stem from the contribution of new degradation products to the absorbance of the suspension. The nature of these degradation products will be explored in the following discussion.

3.3. Degradation mechanisms

To gain insights into the fundamental degradation mechanism of $NbOCl_2$, as shown in Fig. 3a–c, we conducted TEM characterization of $NbOCl_2$ nanosheets that were stored in a water environment for various durations. The pristine $NbOCl_2$ nanosheets can be observed to have lattice streaks at the edges (Fig. 3a). The corresponding high-resolution image (Fig. S9, ESI†) reveals a lattice stripe spacing of 0.34 nm, corresponding to the (101) plane. A slight amorphous region is attributed to air exposure during sample preparation, as confirmed by the inset showing the SAED pattern and elemental mapping. Fig. 3b shows a high-resolution image of $NbOCl_2$ nanosheets exposed to water for 2 h. The disappearance of the Cl element demarcates the crystalline and non-amorphous morphology, which is consistent with the SAED pattern shown in the inset. The central region in Fig. S10a (ESI†) displays lattice stripes, while the corresponding SAED pattern confirms the crystalline nature of the material (opposite to the edges, Fig. S10b, ESI†). Following vacuum annealing (remove H element),[44] EDS mapping (Fig. S11, ESI†) revealed an Nb : O stoichiometric ratio near 1 : 2 in the degraded area, indicating Nb to exist in a +4 valence state. Finally, Fig. 3c displays the morphology of thoroughly degraded nanosheets. Notably, the Cl elements are absent, yet the sheet-like morphology is preserved, suggesting that the Nb–O–Nb structure in the pristine nanosheets was not destroyed, and the position of Cl in the Nb–Cl–Nb structure was changed.[44] It is reasonable to deduce that the progression of the degradation reaction is an irreversible process that initiates

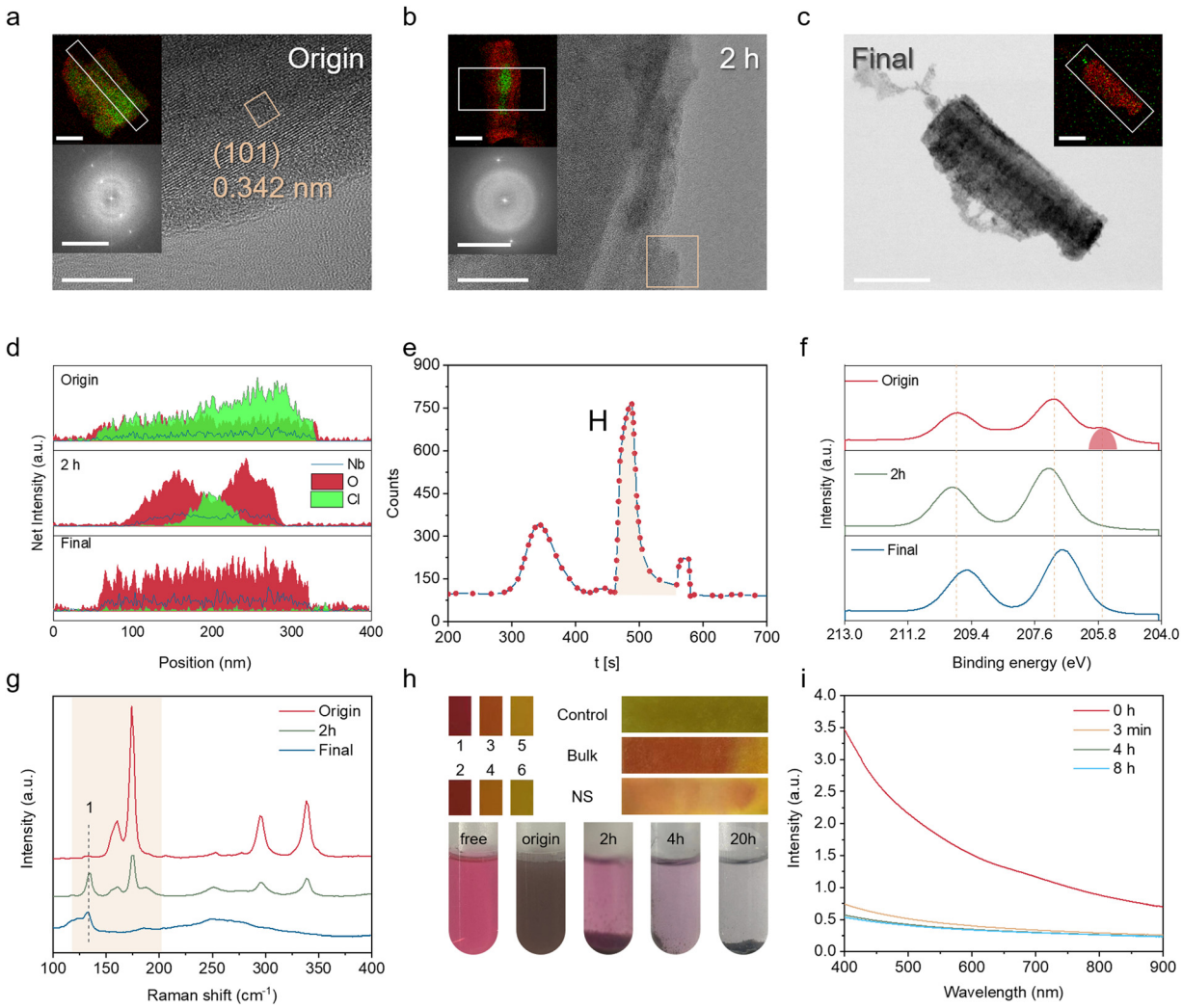

Fig. 3 (a)–(c) TEM images of $NbOCl_2$ nanosheets stored at room temperature and in a water environment for 0 hours (Origin), 2 hours, and the final product, respectively (scale bar: 100 nm). Additionally, the illustration includes an EDS mapping of Cl and O elements (scale bar: 100 nm), complemented by partial representations of selected area electron diffraction patterns (scale bars of *a*: 10 cm^{-1}, scale bar of *b*: 5 cm^{-1}). (d) The net intensity diagrams correspond to the spatial positions of the three elements within the white area depicted in the EDS mapping inserted in images (a)–(c). (e) The elemental H content profile was characterized by passing the final samples through an organic elemental analyzer. (f)–(g) The evolution of Nb 3d high-resolution XPS spectra and Raman spectra with water treatment time. (h) Optical images of $NbOCl_2$ nanosheets and alkaline fuchsine in water at different time intervals, along with the pH values of the reaction solutions. (i) Extinction spectra of $NbOCl_2$ nanosheets dispersed in a robust alkali environment for different times.

from the edges or boundaries and moves toward the center of the nanosheets. During this process, nanosheets with a heterojunction-like structure were formed, where $NbOCl_2$ was in the center and NbO_xH_y ($-2x + y = -4$) was at the edge.

As depicted in Fig. 3d, analyzing the correlation of the content of three elements in the mapping images of the samples reveals that removing the Cl element from the nanosheet is accompanied by a notable increase in oxygen content, such as groups containing oxygen atoms or single oxygen atoms. Therefore, organic element analysis (EA) was used to characterize the hydrogen proportion in the degraded $NbOCl_2$ material, which was found to be 1.2% (Fig. 3e). This indicates that the oxygen-containing OH^- group replaced the chlorine atom during the degradation reaction. XPS characterization was performed on $NbOCl_2$ nanosheets stored in a water environment for various durations to investigate changes in elemental content and valence states during the degradation of $NbOCl_2$ nanosheets (Fig. S12, ESI†). It is evident from the entire XPS spectra that the intensities of Cl 2p and Cl 2s peaks in $NbOCl_2$ nanosheets significantly decrease as the degradation progresses, aligning with the results obtained from element mapping in Fig. 3a–c. It was further confirmed by the fine spectra of Cl 2p and Cl 2s (Fig. S12b, e, ESI†). The changes in the binding energy of the main peaks in the O 1s (Fig. S12c, ESI†) and Nb 4p (Fig. S12f, ESI†) orbitals also reflect the degradation process. As degradation progresses, the peaks near 205.7 eV in the Nb 3d orbit, corresponding to the +4 valence state, disappear (Fig. 3f). Moreover, the peaks near 207.1 and 209.8 eV, which are linked to the V oxidation state or Nb +5 3d orbital, shift to 207.2 and 209.8 eV which are linked to the +5 valence state.[45,46] The final total changes are +5 valency related to 206.8 and 209.5 eV.[47,48] The V oxidation state of the initial sample is related to exposure to air due to limited sample preparation conditions, which is consistent with the fact that Nb oxides are easily oxidized.

The Raman spectral analysis of $NbOCl_2$ nanosheets after degradation reveals the emergence of a new peak (line 1; peak position: 133.2 cm^{-1}), as depicted in Fig. 3g, compared to the initial state. This observation presents a new non-destructive method for identifying degradation in $NbOCl_2$ based on investigating the characteristic peaks in Raman spectra, which are only observable when the material has degraded, as determined experimentally. In Fig. 3h, the pH value of the aqueous solution after degradation was evaluated for both the bulk material (1 mg ml^{-1}) and the nanosheets. Upon achieving the acidic nature of the reaction solution, some bleaching of the pH test paper in the fresh reaction solution was observed. It prompted us to perform an experiment using an alkaline fuchsin solution to assess color stability. After dispersing a significant amount of nanosheets in the fuchsin solution, the color vanished within only 20 hours. It indicated that hypochlorous acid is produced during the degradation reaction of the $NbOCl_2$ nanosheets, which coincides with the speculation in Fig. 2f. After adding $AgNO_3$ solution to the post-degradation reaction mixture, we observed a white substance that was insoluble in water (inset in Fig. S13a, ESI†). Over time, it gradually transitioned to a reddish-brown color, as depicted in Fig. S13a (ESI†). This precipitate was characterized *via* XPS analysis, and the full spectrum revealed an abundance of Ag, Cl, and O elements (Fig. S13b–d, ESI†). The results suggest that the reddish-brown substance was partly AgCl oxidized to Ag_2O. Thus, the degradation of $NbOCl_2$ produces hypochlorous acid, ultimately releasing H^+ and Cl^-.

Furthermore, the primary factors driving the degradation of $NbOCl_2$ nanosheets were investigated. As depicted in Fig. S14 (ESI†), the extinction spectra of nanosheets dispersed in both strong acid and water environments were monitored at various time points with equal concentrations. Within 8 hours, the spectral signal intensity in the robust acidic environment (Fig. S14a, ESI†) was notably higher than that in the control group (Fig. S14b, ESI†), suggesting that a significant presence of H^+ ions can impede the progression of the material degradation reaction. In a robust alkaline environment (Fig. 3i), $NbOCl_2$ nanosheets evidently exhibited decomposition within a short duration, accompanied by dramatic changes in the extinction spectrum, indicating an accelerated degradation reaction driven by OH^-.[44] Based on this evidence, it is believed that the degradation underwent the following chemical processes. The possible chemical reaction equations are as follows:

$$NbOCl_2 + 2H_2O + O_2 \rightarrow 2HClO + NbO(OH)_2$$

$$2HClO \rightarrow 2HCl + O_2$$

$$4NbO(OH)_2 + O_2 \rightarrow 2Nb_2O_3(OH)_4$$

3.4. Improvement in the SHG stability

$NbOCl_2$ nanosheets prepared by LPE retain excellent SHG properties at λ_{SHG} = 400 nm ($\eta = 1.1 \times 10^{-5}$%, 1 mw), as demonstrated in Fig. 4a. In polar coordinates, the relationship between the SHG intensity of $NbOCl_2$ flakes and the excitation polarization angle exhibits a dumbbell-shaped angular dependence pattern.[6] The influence of polarization effects can be neglected when investigating the stability of the nanosheet morphology. A stability test was conducted on $NbOCl_2$, which generated the SHG intensity *in situ* under atmospheric and PMMA conditions (Fig. 4b). The results showed that after $NbOCl_2$ was exposed to air, the SHG intensity significantly decreased by 69% after 48 min (Fig. 4c). After 720 minutes, the SHG intensity of $NbOCl_2$ in the air environment decreased, and remained at only 1.6% of its initial value, while the SHG intensity in the PMMA environment showed no significant variation. The isolation of $NbOCl_2$ from water and oxygen by PMMA helped maintain structural stability, which in turn, did not lead to a significant reduction in SHG strength. These results further support the conclusions of the investigation of the degradation mechanism. As the degradation process progresses, the SHG signal intensity of $NbOCl_2$ gradually decreases, suggesting a change in structural symmetry.[6] Even after complete degradation (final), faint SHG signals are retained (collection time 5 s), which are reduced 1000 times compared to the original group, as illustrated in Fig. S15 (ESI†). On the log scale, the SHG intensity of $NbOCl_2$ (Origin) as a function of pump power was fitted and plotted with a slope

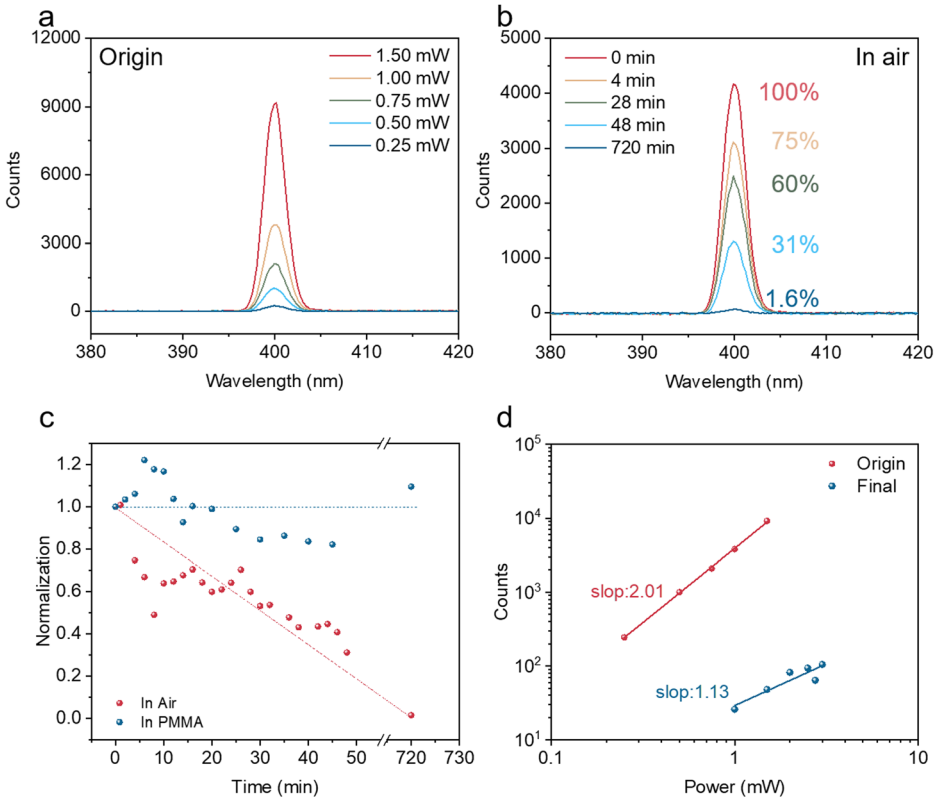

Fig. 4 (a) Excitation power-dependent SHG spectrum of the Origin group (collection time: 1s). (b) SHG stability of $NbOCl_2$ nanosheets after various durations in the air environment. (c) SHG peak intensity of $NbOCl_2$ in air and PMMA as a function of time. (d) A logarithmic-scale representation of the SHG intensity against excitation power is depicted for the Origin and the Final group. The slope of the linear fit for the Origin group is equal to 2.01, affirming the second-order characteristics inherent to the ensuing nonlinear signal.

equal to 2.01, revealing the quadratic power dependence of the SHG signal on the pump power (Fig. 4d). The Final sample was fitted and plotted with a slope of 1.13, indicating weaker SHG efficiency due to the lower signal-to-noise ratio. The numerical value of the slope could be utilized to assess the impurities caused by degradation in the sample. These findings suggest that $NbOCl_2$ nanosheets prepared by LPE retain remarkably ultrafast nonlinear SHG response. Nevertheless, rapid degradation upon exposure to air or water presents a significant challenge for the future practical applications of $NbOCl_2$. Enhancing the stability of $NbOCl_2$ in aqueous solutions and natural environments will be a crucial research focus for its future applications. The application of artificial intelligence in nonlinear optics is gradually increasing. However, the underdevelopment of the model dimensions led to large error values between the predictions and the experimental values in some aspects.[49] These results provide new ideas to improve the model to increase its usefulness.

4 Conclusions

In summary, we have revealed the kinetic degradation mechanism of $NbOCl_2$ nanosheets and demonstrated enhanced SHG response stability at the nanoscale by a PMMA isolation protection strategy. In liquid-phase environments, OH^- ions lead to rapid degradation and dissociation of nanosheets from the edges. Excessive H^+ ions significantly inhibit the degradation of the $NbOCl_2$ nanosheets, which is reflected in the extinction spectra. Long-term storage stability of up to three months is demonstrated in anhydrous NMP environments. While the ultra-strong SHG performance of $NbOCl_2$ gradually diminishes with prolonged degradation, a faint response is ultimately retained. In air environments, PMMA isolation protection is necessary to maintain excellent SHG response over extended periods. Our results provide deeper insights into the degradation kinetics of $NbOCl_2$ nanosheets and offer meaningful references for future nonlinear optical device design.

Data availability

The data supporting this article have been included as part of the ESI.†

Conflicts of interest

There are no conflicts to declare.

Acknowledgements

This research was supported by the National Natural Science Foundation of China (Grant No. 52227806, 62275275, 11904239), the National Key R&D Program of China (Grant No. 2023YFC3906103), and the Natural Science Foundation of Hunan Province (Grant No. 2021JJ40709, 2022JJ20080). This work was also supported in part by the High-Performance Computing Center of Central South University and the Open Sharing Fund for the Large-scale Instruments and Equipment of Central South University. The authors thank Dr Wenli Bao for the valuable discussions.

Notes and references

1 H. Li, Z. Wang, L. Wang, Y. Tan and F. Chen, *Light: Sci. Appl.*, 2023, **12**, 223.
2 S. Borówka, U. Pylypenko, M. Mazelanik and M. Parniak, *Nat. Photonics*, 2024, **18**, 32–38.
3 Q. Guo, X.-Z. Qi, L. Zhang, M. Gao, S. Hu, W. Zhou, W. Zang, X. Zhao, J. Wang and B. Yan, *Nature*, 2023, **613**, 53–59.
4 D. Jayachandran, R. Pendurthi, M. U. K. Sadaf, N. U. Sakib, A. Pannone, C. Chen, Y. Han, N. Trainor, S. Kumari and T. V. Mc Knight, *Nature*, 2024, **625**, 276–281.
5 T. Fu, K. Bu, X. Sun, D. Wang, X. Feng, S. Guo, Z. Sun, Y. Fang, Q. Hu and Y. Ding, *J. Am. Chem. Soc.*, 2023, **145**, 16828–16834.
6 I. Abdelwahab, B. Tilmann, X. Zhao, I. Verzhbitskiy, R. Berté, G. Eda, W. L. Wilson, G. Grinblat, L. de, S. Menezes and K. P. Loh, *Adv. Opt. Mater.*, 2023, 2202833.
7 J. Fu, N. Yang, Y. Liu, Q. Liu, J. Du, Y. Fang, J. Wang, B. Gao, C. Xu and D. Zhang, *Adv. Funct. Mater.*, 2024, **34**, 2308207.
8 T. Su, C. H. Lee, S.-D. Guo, G. Wang, W.-L. Ong, L. Cao, W. Zhao, S. A. Yang and Y. S. Ang, *Mater. Today Phys.*, 2023, **31**, 101001.
9 Y. Jia, M. Zhao, G. Gou, X. C. Zeng and J. Li, *Nanoscale Horiz.*, 2019, **4**, 1113–1123.
10 C. Liu, X. Zhang, X. Wang, Z. Wang, I. Abdelwahab, I. Verzhbitskiy, Y. Shao, G. Eda, W. Sun and L. Shen, *ACS Nano*, 2023, **17**, 7170–7179.
11 R. E. Peierls, *Quantum theory of solids*, Oxford University Press, 1955.
12 Y. Fang, F. Wang, R. Wang, T. Zhai and F. Huang, *Adv. Mater.*, 2021, **33**, 2101505.
13 L. Pan, Y.-L. Wan, Z.-Q. Wang, H.-Y. Geng and X.-R. Chen, *J. Appl. Phys.*, 2023, 134.
14 M. I. Zappia, G. Bianca, S. Bellani, M. Serri, L. Najafi, R. Oropesa-Nuñez, B. Martín-García, D. Bouša, D. Sedmidubský and V. Pellegrini, *Adv. Funct. Mater.*, 2020, **30**, 1909572.
15 M. Huang, S. Luo, H. Qiao, B. Yao, Z. Huang, Z. Wang, Q. Bao and X. Qi, *Small Sci.*, 2024, 2300246.
16 L. Ye, W. Zhou, D. Huang, X. Jiang, Q. Guo, X. Cao, S. Yan, X. Wang, D. Jia and D. Jiang, *Nat. Commun.*, 2023, **14**, 5911.
17 N. Zhang, N. Li, L. Wang, M. Sun and J. Wang, *J. Mol. Struct.*, 2024, **1299**, 137064.
18 D. Hanlon, C. Backes, E. Doherty, C. S. Cucinotta, N. C. Berner, C. Boland, K. Lee, A. Harvey, P. Lynch and Z. Gholamvand, *Nat. Commun.*, 2015, **6**, 8563.
19 W. Du, X. Jiang and L. Zhu, *J. Mater. Chem. A*, 2013, **1**, 10592–10606.
20 J. H. Han, S. Lee, D. Yoo, J.-H. Lee, S. Jeong, J.-G. Kim and J. Cheon, *J. Am. Chem. Soc.*, 2013, **135**, 3736–3739.
21 C. Backes, B. M. Szydłowska, A. Harvey, S. Yuan, V. Vega-Mayoral, B. R. Davies, P.-L. Zhao, D. Hanlon, E. J. Santos and M. I. Katsnelson, *ACS Nano*, 2016, **10**, 1589–1601.
22 V. Nicolosi, M. Chhowalla, M. G. Kanatzidis, M. S. Strano and J. N. Coleman, *Science*, 2013, **340**, 1226419.
23 H. Schnering and H. Wöhrle, *Angew. Chem.*, 1963, **75**, 684.
24 H. Hillebrecht, P. Schmidt, H. Rotter, G. Thiele, P. Zönnchen, H. Bengel, H.-J. Cantow, S. Magonov and M.-H. Whangbo, *J. Alloys Compd.*, 1997, **246**, 70–79.
25 M. Bortoluzzi, E. Ferretti, F. Marchetti, G. Pampaloni, C. Pinzino and S. Zacchini, *Inorg. Chem.*, 2016, **55**, 4173–4182.
26 H. Schäfer and F. Liedmeier, *Z. Anorg. Allg. Chem.*, 1964, **329**, 225–228.
27 J. Kang, J. D. Wood, S. A. Wells, J.-H. Lee, X. Liu, K.-S. Chen and M. C. Hersam, *ACS Nano*, 2015, **9**, 3596–3604.
28 Y. Wu, I. Abdelwahab, K. C. Kwon, I. Verzhbitskiy, L. Wang, W. H. Liew, K. Yao, G. Eda, K. P. Loh and L. Shen, *Nat. Commun.*, 2022, **13**, 1884.
29 Y. Li, L. Shi, X. Gao, J. Wang, Y. Hu, X. Wu and Z. Wen, *Chem. Eng. J.*, 2021, **421**, 127853.
30 F. Xiao, K. Wang and M. Zhan, *Appl. Surf. Sci.*, 2010, **256**, 7384–7388.
31 J. Cao, J. Li, W. Chu and W. Cen, *Chem. Eng. J.*, 2020, **400**, 125813.
32 J. Zhu, F. Chen, J. Zhang, H. Chen and M. Anpo, *J. Photochem. Photobiol., A*, 2006, **180**, 196–204.
33 W. Mu, X. Xie, X. Li, R. Zhang, Q. Yu, K. Lv, H. Wei and Y. Jian, *RSC Adv.*, 2014, **4**, 36064–36070.
34 J. Y. Cheong, C. Kim, J. W. Jung, K. R. Yoon, S. H. Cho, D. Y. Youn, H. Y. Jang and I. D. Kim, *Small*, 2017, **13**, 1603610.
35 X. Wang and G. Shen, *Nano Energy*, 2015, **15**, 104–115.
36 V. Atuchin, I. Kalabin, V. Kesler and N. Pervukhina, *J. Electron Spectrosc. Relat. Phenom.*, 2005, **142**, 129–134.
37 A. V. Kovalevsky, M. H. Aguirre, S. Populoh, S. G. Patrício, N. M. Ferreira, S. M. Mikhalev, D. P. Fagg, A. Weidenkaff and J. R. Frade, *J. Mater. Chem. A*, 2017, **5**, 3909–3922.
38 Z. Yang, X. Lu, W. Tan, J. Zhao, D. Yang, Y. Yang, Y. He and K. Zhou, *Appl. Surf. Sci.*, 2018, **439**, 1119–1126.
39 C. Backes, R. J. Smith, N. McEvoy, N. C. Berner, D. McCloskey, H. C. Nerl, A. O'Neill, P. J. King, T. Higgins and D. Hanlon, *Nat. Commun.*, 2014, **5**, 4576.
40 L. Yadgarov, C. L. Choi, A. Sedova, A. Cohen, R. Rosentsveig, O. Bar-Elli, D. Oron, H. Dai and R. Tenne, *ACS Nano*, 2014, **8**, 3575–3583.
41 F. Cao, Y. Zhang, H. Wang, K. Khan, A. K. Tareen, W. Qian, H. Zhang and H. Ågren, *Adv. Mater.*, 2022, **34**, 2107554.
42 W. Yu, J. Li, T. S. Herng, Z. Wang, X. Zhao, X. Chi, W. Fu, I. Abdelwahab, J. Zhou and J. Dan, *Adv. Mater.*, 2019, **31**, 1903779.

43 J.-S. Oh, X. Fang, T.-H. Kim, M. Lynn, M. Kramer, M. Zarea, J. A. Sauls, A. Romanenko, S. Posen and A. Grassellino, *Appl. Surf. Sci.*, 2023, **627**, 157297.
44 L. Yu, H. Li, H. Shang, P. Xing, B. Zhou, Z. Chen, X. Liu, H. Zhang, Y. Shi and L. Zhang, *ACS Nano*, 2023, **17**, 15077–15084.
45 J. Dash, L. Chen, M. R. Topka, P. H. Dinolfo, L. Zhang, K. Kisslinger, T.-M. Lu and G.-C. Wang, *RSC Adv.*, 2015, **5**, 36129–36139.
46 Y. Wang, A. Chen, S. Lai, X. Peng, S. Zhao, G. Hu, Y. Qiu, J. Ren, X. Liu and J. Luo, *J. Catal.*, 2020, **381**, 78–83.
47 H. Brunckova, M. Kanuchova, H. Kolev, E. Mudra and L. Medvecky, *Appl. Surf. Sci.*, 2019, **473**, 1–5.
48 X. Jin, Y. Deng, H. Tian, M. Zhou, W. Tang, H. Dong, X. Zhang and R. Liu, *Green Energy Environ.*, 2024, **9**(8), 1257–1266.
49 J. Z. García-Córdova, J. A. Arano-Martinez, C. Mercado-Zúñiga, C. L. Martínez-González and C. Torres-Torres, *AI*, 2024, **5**, 2203–2217.